Foam stability of 3D printable lightweight foamed concrete

Seung Cho[1*], Algurnon van Rooyen[1], Elsabe Kearsley[2], Gideon van Zijl[1]

[1-] Division for Structural Engineering and Civil Engineering Informatics, Department of Civil Engineering, Stellenbosch University, Stellenbosch, 7600, South Africa

[2-] Department of Civil Engineering, University of Pretoria, South Africa

*Corresponding author email: scho@sun.ac.za

Foam Stability of 3D Printable Lightweight Foamed Concrete

This study investigates the susceptibility of precursor foam in 3D printable foamed concrete (3DP-FC), particularly in aspects of rheology. The relatively higher yield stress, film liquid withdrawal from unsaturated cement grains and the pumping process raise a concern of considerable foam degradation. Foam stability under the static and dynamic environment is investigated with a wide yield stress range of the base mix (200 - 1500 Pa) and foamed concrete density range (700 - 1400 kg/m^3) is investigated in this study. No major foam instability was found in the static environment with comparison of various wet-to-dry density and porosity models, while the pumping process caused densification for the higher density 3DP-FC. Other than the gravimetric measurements, the X-ray CT scans were performed to analyse the porosity, sphericity and pore distribution changes between the pre- and post-pumped samples. This paper addresses the effect of fluidity on foam stability due to physicochemical interaction on microstructural level, and the producibility of a stable 3DP-FC with a density as low as 700 kg/m^3

Highlights

- An extensive interdisciplinary foam stability theory and solid-bubble interactions are discussed.
- Foam stability secured 3D printable foamed concrete with wide density range is developed.
- Rheology-based foam stability study including 3DCP process is assessed.
- Actual 3DCP setup was employed to perform foam stability assessment of post-pumped specimen.

Keywords: Foamed concrete; 3D printed concrete; foam stability; void structure; digitally fabricated concrete

1 Introduction

Foamed concrete (FC) normally consists of a cement paste or mortar that is aerated with a foaming agent to reduce the density of the material, resulting in a thermally efficient building material. The air voids are introduced to the mortar by an aqueous foam addition and the foam stability in the pseudo-solid or elastoplastic material until the matrix is hardened is a crucial aspect for quality control. Stability of the foam is not only dependent on the shape and the size of the bubbles in the foam, which are determined by the type of foaming agent and production procedure, but also on the rheology of the paste surrounding the air bubbles [1].

The development of an extrusion-based digital construction technique, widely known as 3D concrete printing (3DCP), introduces an automation in construction allowing construction time and cost reduction, equipping highly skilled workforces and architectural design flexibility as no formwork is involved [2]. Despite problems with reinforcement and standardisation, 3DCP is unquestionably seen to shift the paradigm shortly in the traditional construction sector thanks to the tireless involvement from academia, industry, public and government. Along the innovation, there are a few attempts to hybridise 3DCP with FC [3–5], to lessen the dead load of the structure and to promote energy efficiency. For instance, Cho *et al.* [3] showed a 3D printed FC buoyant modular façade element as a prototype for a practical application, such as exterior cladding which can be found in Fig. 1. The lightweight nature eased manual handling, installing as well as self-weight induced loading to the parental structure. Those studies showed potential, but further research is required to ensure that the air voids in the FC can sustain the mechanical agitation and 3D printer's pumping pressure.

(a) (b) (c)

Fig. 1. 3D printing in FC. (a) Fresh FC after mini-slump cone is lifted showing a sound shape retention; (b) the printed object at the completion; and (c) a prototype for an exterior cladding with the 3D printed façade elements.

In this paper foam stability with various foam volume fractions, i.e. different densities, and the effect of pumping on the stability of the voids are investigated. The first part of the paper investigates the influence of rheology of base mortar mix on the foam stability. A stable base mix with most favourable constructability of 3DCP is selected based on the first part of the study. The base mix is then used to produce three different densities of 3DP-FCs by varying foam volume fraction for the second part of the study. Prepared fresh concretes were fed into a positive displacement 3D concrete pump and the gravimetric measures of pre- and post-pump densities were recorded. A physicochemical solid-bubble interaction between bubble film and the unsaturated cement grain at adsorption is discussed for the

dominating foam destruction mechanism, coalescence. Also the continuous change in fluidity due to the released liquid from the bubble film at foam degradation is hypothesised for an equilibrium state in which a new term, *ideal fluidity*, is defined in this study. Pre- and post-3D printed FC void structures are compared via X-ray computed tomography (X-CT) as well as theoretical porosity calculation models from literature.

2 Background on foam stability

A diluted aqueous surfactant solution flows through a mechanical agitation process with high air pressure to produce a precursor aqueous foam. In the system of aqueous foam, the amphiphilic surfactant molecules populate and adsorb around air-liquid interface, at nanometre scale, with the hydrophobic parts in contact with air which creates a thin film, i.e. the surface of micelle, separating the individual bubbles having size range of micrometre to centimetre [6]. When the thin films are in contact, a liquid skeleton of interconnected channels at the junction points are created by a substantial Laplace pressure difference between the gas and the liquid phase due to the small bending radius of a bubble, known as the Plateau border [7]. Foam comprises the network of bubbles and the physical and physicochemical properties of foam are mainly dictated by the properties of the lower length-scales [6].

Since all foams are thermodynamically unstable [8], foam destabilises over time, so-called foam ageing, with the following mechanisms: (1) *drainage* of gravity-driven liquid flow leading to the separation of the gas and the liquid, (2) *ripening* or *coarsening* where gas diffusion occurs between different size of bubbles due to the differential Laplace pressures, and (3) *coalescence* which is a merging process of bubbles by film rupture at a critical thickness [6]. It should be mentioned the three mechanisms are not discrete, but rather interdependent [9].

The liquid film thickness reduces over time. This film thinning process continues until it reaches a metastable equilibrium state, and highly influences the foam stability or the destabilisation rate. Intrinsic physical and physicochemical properties of bubbles, such as surface tension, surface rheology, and film elasticity are mainly determined by the solution concentration and type of surfactant [10], but also surface forces which can be explained by a classical DLVO theory (after Derjaguin, Landau, Verwey,

and Overbeek) [11], control the film thinning process. The theory explains the aggregation of dispersed particles in a liquid medium is maintained by the force balance primarily between two forces, the attractive van der Waals force and the repulsive electrostatic double-layer force [7,8,11]. The balanced surface forces develop a pressure within the liquid lamella to determine the metastable film thickness. The pressure difference between the pressure developed within the film and the applied bulk pressure, called disjoining pressure (Π_d), is defined as the change in Gibbs free energy per unit area with respect to lamella thickness [12]. Both attractive and repulsive surface forces change over the distance between particles. The disjoining pressure can be expressed in terms of film thickness, h. An idealised disjoining pressure isotherm is depicted in Fig. 2.

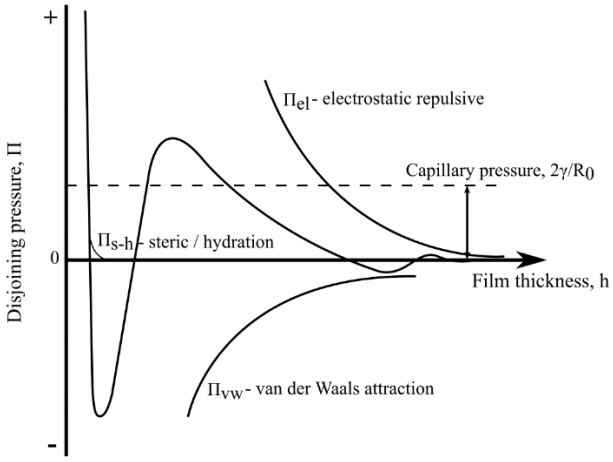

Fig. 2. Idealised disjoining pressure isotherm. Re-worked from [13].

In an aqueous foam, i.e. two phase system, a (Laplace) capillary pressure, P_σ, develops based on the bubble size and surface tension. The pressure competes with the disjoining pressure to determine the driving pressure, ΔP, leading to the formation of an equilibrium film. The pressure balance gives

$$\Delta P = P_\sigma - \Pi_d \tag{1}$$

When the aqueous foam is incorporated into a cementitious paste, it becomes a three-phase system, and the foam destabilisation mechanism in the bulk material is subtly modified as the concrete paste separates individual bubbles due to the high solid concentration. The foam bubble is surrounded by the solid paste, i.e. adsorption due to the interplaying surface forces, and the complex solid-bubble interaction takes part in the stability of foam. A bubble and solid particle approach each other with

velocity inducing kinetic energy (*collision*) during a stable cement grain-bubble agglomeration formation (*attachment*) [6,9]. At an attachment state, the bubble is suppressed by the bulk solid paste and the suppressing pressure, or more common term 'confinement pressure' and denoted as P_c, depending on the bulk density, viscosity and yield stress of solid paste [14]. Then the pressure balance equation becomes

$$\Delta P = P_c + P_\sigma - \Pi_d \quad (2)$$

To make FC 3D printable, there is a rheological requirement of sufficiently high static shear yield stress development rate for shape retention and buildability during the construction phase. Cho *et al.* [3] performed a comprehensive rheological characterisation and buildability assessment of 3DP-FC. The study showed that FC with the density of 700 kg/m^3 and an initial static yield stress of 350 Pa achieved a sound shape retention at rest as well as a certain extent of buildability. Another rheology characterisation study of 3DP-FC by Markin *et al.* [15] presents a similar result for cases where the yield stress is higher than 300 Pa for the density of 1200 kg/m^3. Aqueous foam incorporation tends to decrease the static and dynamic yield stress of the base mix [16]. Hence, the yield stress of the base mix is expected to be higher than the abovementioned rheological requirement.

Several studies found that high static yield stress of solid paste can theoretically retard or completely arrest the drainage and the ripening destabilisation mechanisms by capturing the mobility of a bubble completely [1,6]; however, the high static yield stress also increases the confinement pressure which may lead to significant bubble breakage by film rupture or coalescence of bubbles.

Pumping is a crucial process in the 3D concrete printing technique. It is widely known that pumping pressure results in the loss of air content, approximately 1% - 1.5% air content loss in case of a conventional concrete [17,18]. During concrete material transport to the targeted height or position via a progressive cavity pump which is the most common concrete pumps in 3DCP, pumping pressure builds up within the transporting channel (e.g. pipe), so does internal pressure of the concrete matrix. The pumping pressure is dependent on various factors, e.g. rheology of the bulk material, pipe geometry, and flow rate, but the pumping pressure is generally expected to be 70 kPa (0.7 bar) or higher for 3DCP [19,20]. The pumping pressure, P_P, is added on the right-hand side in Eq (2), leading to

$$\Delta P = P_c + P_\sigma + P_P - \Pi_d \quad (3)$$

Several studies have investigated foam stability in cementitious materials with rheological approach. Kearsley *et al.* [21] proposed a modified hydraulic flow turntable test, a fluidity range of the base mortar mix, expressed as a slump flow including 15 strokes at a height of 12.7 mm of 220 – 250 mm, for stable FC production. The authors postulated the degree of saturation of cement grain affects foam stability due to water withdrawal from the film during hydration, which may cause bubble film rupture. Feneuil *et al.* [1,22] established a rheological investigation of cement paste for stable morphology-controlled cement foam production and a foam stability criterion. The studies found a bubble size-dependent destabilisation mechanism in which drainage and ripening are the principal mechanisms and foam instability was found when the yield stress was greater than 10 Pa (up to 100 Pa was considered in the study). However, it is worthwhile to mention that cement foam and FC must be distinguished because of the substantial solid fraction difference.

3 Experimental programs

3.1 Materials and mix design

FC mix design is not standardised to date, but several researchers take consideration of the target wet density (ρ_t) as prime design factor [21,23,24]. Kearsley *et al.* [21] proposed a FC mix design based on the mass and volume balances of constituents with two variables, the cement content (c) in kg/m^3 and foam volume content (V_f) in m^3. The sum of dry constituents, free water (w) and foam mass ($RD_f.V_f$) with *RD* denoting relative density dictate the first equation, Eq. (4). This must be balanced with the prime design factor, i.e. target density in the fresh state. The second equation, Eq. (5), is to consider the unit volume (1 m^3) which is equal to the total volume of the entire composition of constituents.

$$\rho_t = c + c \cdot w_c + RD_f \cdot V_f \quad (4)$$

$$1 = c/RD_c + c \cdot w_c + V_f \quad (5)$$

These equations can be expanded as additional ingredient materials, such as supplementary cementitious materials (SCMs), and inert materials are included. In this study, the mix design includes

calcium sulphoaluminate (*CSA*) cement, fly ash (*a*), silica fume (*sf*), graded fine silica sand (*s*) and nano-silica powder (*nS*) to improve the material performance in both fresh and hardened states [21,25,26]. The modified FC mix design equations are described in the following equations.

$$\rho_t = c \cdot [\alpha + \beta] + RD_f \cdot V_f \quad (6)$$

$$1 = c \cdot [\beta + \gamma] + V_f \quad (7)$$

where

$$\alpha = 1 + (CSA/c) + (a/c) + (s/c) + (sf/c) + (nS/c)$$

$$\beta = w_c + w_{CSA} \cdot (CSA/c) + w_a \cdot (a/c) + w_s \cdot (s/c) + w_{sf} \cdot (sf/c) + w_{nS} \cdot (nS/c)$$

$$\gamma = \frac{1}{RD_c} + \frac{(CSA/c)}{RD_{CSA}} + \frac{(a/c)}{RD_a} + \frac{(s/c)}{RD_s} + \frac{(sf/c)}{RD_{sf}} + \frac{(nS/c)}{RD_{nS}}$$

Please note that *w* with subscript refers to water demand to each dry constituent, and *CSA/c*, *a/c*, *s/c*, *sf/c* and *nS/c* are predetermined mass ratio variables.

To determine the two primary variables, *c* and V_f, the water demand and mass proportion to cement content of each dry material are predetermined. The water demand determination can be performed by an modified ASTM C1437 flowtable test [27] according to [21]. The water demand of each dry constituent can be determined by a sensitivity analysis approach until the mixture of water and dry material has a 220 mm flow table spread diameter after 15 strokes. For ingredient materials that are not pozzolanic or cementitious, cement is added for the process of determining their water demand. The water-to-cement (w_c) and water-to-fly ash (w_a) ratios were kept above 0.3 and 0.25 respectively according to literature [21]. For the mix design determination throughout the study, the water demand of fly ash was the only variable to change the consistency of the fresh mix.

CSA cement was introduced into the mix design, since the partial CSA substitution in FC was found to improve foam stability by rapid early strength development through a high ye'elimite (C_4A_3S) content in sulfoaluminate belite and ferrialuminate clinkers [14]. This property is also expected to improve the thixotropy rate, and thereby also the buildability of 3DP-FC.

The selected cement contains 6 – 20% limestone extenders and is classified as CEM II/A-L 52.5N. The locally sourced fly ash, called Durapozz, is categorised as class F. Both conform to SANS 50197-1 [28]. Nano silicon dioxide powder with an average particle size of 30 ± 5 nm was selected as extender together with Chryso densified silica fume. Graded silica sand was used as an inert material and has a maximum particle size of 0.5 mm. High aluminate content CSA cement (type III) manufactured by Royal White Cement (RWC) is added in a fixed CSA-to-cement ratio of 10%. The synthetic fibre type for fibre reinforcement is 6 mm long polypropylene (PP) fibre. A summarised water demand and proportion to cement content is presented in Table 1, and chemical and physical constituents are summarised in Table 2 and Table 3 respectively.

Table 1. Water demand and proportions to cement content for 3DP-FC mix design.

Materials	Cement	CSA	Fly ash	Sand	Silica fume	Nano silica	PP fibre
Water demand	0.375	0.375	*Variable**	0.08	0.71	0.84	**0.4% of total mix volume
Ratio to cement content	1.0	0.1	1.0	0.2	0.1	0.02	

**The range of w_a was between 0.25 and 0.38.*
***No added water for fibre.*

Table 2. Chemical composition (in mass percentages) of pozzolanic materials.

	SiO_2	Al_2O_3	Fe_2O_3	CaO	MgO	K_2O	Na_2O	TiO_2	SO_3
Cement	21.5	5.5	3	65.5	2.0	<0.5	<0.5	-	1.5
CSA	10.5	34	2.5	42.5	3.5	-	-	1.5	8.5
Fly ash	54.1	31.8	3.2	4.9	1.2	0.8	0.2	1.7	-
Silica Fume	99.5	<0.1	<0.1	<0.1	<0.1	-	-	-	-

Table 3. Physical properties of the dry constituents, with *RD* the relative density and *SA* the specific surface area.

Materials	OPC	CSA	Fly ash	Silica Fume	Nano SiO_2	Sand	PP fibre
RD (-)	3.15	3.1	2.2	2.9	2.17	2.65	0.91
SA (m^2/kg)	400	480	300 - 400	13 000 – 20 000	200 000	97.9	

A protein based foaming agent is diluted by a 1:40 ratio with water and then ferrous sulphate in a 1:80 ratio with water mass is added as a foam stabiliser. The solution undergoes mechanical agitation with a

flow rate of 1 – 3 litres per second and air pressure of 50 – 60 kPa to generate precursor aqueous foam, with a controlled density of 75 ± 5 kg/m^3, according to the specification of the manufacturer. It is worthwhile to mention that a constant type and concentration of surfactant is used throughout the current study.

The foam stability assessment in this study is divided into two stages, considering: (1) the influence of rheology of the base mix without the pumping process and (2) the influence of a continuous and dynamic disturbance from the pump pressure to FC with target densities, 700, 1000 and 1400 kg/m^3, produced with the selected optimal base mix from the first stage.

From Section 2, the lower bound of slump flow for stable conventional FC is 220 mm, but it is worthwhile to investigate the foam stability in less flowable base mixes, i.e. smaller slump flow, to secure a degree of buildability for FC. In the first stage, three base mix designs with different slump flows after 15 strokes were prepared by varying w_a, namely 220 mm, 200 mm, and 180 mm, allowing ±5 mm tolerance of each. These samples are denoted BM220, BM200, and BM180. Additionally, another base mix with CSA cement was designed, denoted BM180CSA, to accelerate the yield stress evolution rate, and the slump flow of the fourth sample to agree with the smallest slump flow of the three, i.e. 180 mm.

A stable and optimal base mix design for constructability of a digital construction application was selected for the following stage. The final test set comprises of 3DP-FCs with target densities of 700, 1000 and 1400 kg/m^3, named TD-7, TD-10, and TD-14, respectively. This test set was subjected to a pump process to assess the foam stability under a high-pressure environment. The set of mix designs are summarised in Table 4, noting that 4.1 kg/m^3 (0.45% of the mixture volume) PP fibres were added of to all mixes. The concrete mixing procedure with a constant mixing speed of 25 rpm in a 50 L pan mixer is presented in Table 5.

Table 4. Mix designs (units are in kg/m^3 except for the ratio w_a).

	BM180	BM180CSA	BM200	BM220	TD-7	TD-10	TD-14
w_a	*0.25*	*0.28*	*0.32*	*0.35*	*0.33*	*0.30*	*0.28*
Cement	452.8	429.3	443.0	438.9	199.5	297.9	429.3
Fly ash	452.8	429.3	443.0	438.9	199.5	297.9	429.3
CSA	-	42.9	-	-	20.0	29.8	42.9

Silica fume	45.3	42.9	44.3	43.9	20.0	29.8	42.9
Sand	90.6	85.9	88.6	87.8	39.9	59.6	85.9
nSiO2	9.1	8.6	8.9	8.8	4.0	6.0	8.6
Water	330.0	341.8	353.8	363.7	168.8	243.2	341.8
Foam	19.6	19.3	18.5	18.0	48.4	35.9	19.3

Table 5. Mixing procedure breakdown.

Step	Duration (min:s)	Action
1	02:00	Mix dry constituents only except for PP fibre
2	05:00	Pour water in the mixing container and mix thoroughly
3	02:00	Add PP fibre in the mixing container mix thoroughly
4	05:00	Add freshly prepared wet foam in the mixing container and mix thoroughly
5	02:00	Measure wet density. If wet density is higher than the tolerance, add more foam and repeat step 4. If wet density is lower than the tolerance, discard the sample.

3.2 Rheometer measurement

The fundamental rheological property of the base mix is characterised by a rotational concrete rheometer manufactured by the International Centre for Aggregate Research (ICAR). The rheometer is composed of a 20-L high-quality stainless-steel container, a driver head with a torque range of 0.01 – 20 N.m and rotational speed range of 0.01 – 0.60 rps, and a four-blade vane welded to a concentric shaft. An anti-slippage mechanism is provided along the container wall by a series of the equally spaced vertical strips.

Constant Shear Rate (CSR) testing was performed by conducting the stress growth test over a single batch for 60 s which measures the torque values over time and automatically selects the maximum torque measured during the test. The maximum torque value is equivalent to static yield stress, denoted as τ_s, refers the maximum shear capacity to initiate a flow, and the post converged, and plateaus at a depreciated torque value implying the dynamic yield stress, denoted as τ_d, depicts the minimum stress required for maintaining flow. The torque values can be converted into shear stress values by the following equation as per the instruction [29]:

$$\tau = \frac{2T}{\pi D^3 \left(\frac{H}{D} + \frac{1}{3}\right)} \quad (8)$$

where T is measured torque (N.m), D is the vane diameter (m), and H is the vane height (m).

A time-dependent rheological parameter, thixotropy, is also a crucial property in rheological performance of a cementitious material. Roussel [30] proposed a simple thixotropy model for fresh concretes by assuming a constant shear strength evolution from the hysteresis loop, called A_{thix}, i.e. the shear yield stress at rest develops linearly with time. Kruger *et al.* [31] proposed a modification of the model to generate a bi-linear relationship between shear strength evolution and time. The latter model captures the rapid initial shear yield stress development rate, defined as R_{thix}, due to the dominant physical interparticle play, i.e. flocculation process.

The modified thixotropy model to evaluate R_{thix} and A_{thix} can be obtained by a series of CSR tests with incremented resting time gap as per [30,31]. To simulate the agitation speed in a pump of the particular 3D concrete printer used for this research, a constant rotational vane speed of 0.2 rps was applied, which is equivalent to a shear rate ($\dot{\gamma}$) of 1.0 s^{-1}. The resting time gap series comprised of 0, 10, 20, and 30 minute intervals. From the set of test results, the thixotropic parameters, R_{thix} and A_{thix}, can be calculated using the following equation:

$$\tau(t) = \begin{cases} \tau_{D,i} + R_{thix} \cdot t & t \leq t_{rf} \\ \tau_{S,i} + A_{thix} \cdot \left(t - t_{rf}\right) & t > t_{rf} \end{cases} \quad (9)$$

where $\tau_{D,i}$ is an initial dynamic yield stress, $\tau_{S,i}$ is an initial static yield stress, and t_{rf} is re-flocculation time defined as $t_{rf} = (\tau_{S,i} - \tau_{D,i})/R_{thix}$.

Furthermore, the Bingham parameters, dynamic yield stress ($\tau_{d.0}$) and plastic viscosity (μ_p), were determined by a flow curve test. A breakdown pre-shear was imposed at 2.5 s^{-1} shear rate for 20 s to generate a consistent shear history to the sample as per the manufacturer's instruction. After the initial breakdown, the shear stresses were measured at 7 equally divided shear rate steps in descending order between the initial shear rate of 2.5 s^{-1} and the final shear rate of 0.25 s^{-1} for 5 s at each step. It must be mentioned the dynamic yield stress can be obtained by both stress growth and flow curve tests [32], however the latter test generates a dynamic yield stress in an equilibrium state, i.e. dynamic yield stress

at a zero-strain rate, where yield stress varied according to an applied shear strain rate. Thus, dynamic yield stress generated by flow curve test is only reported throughout this study.

3.3 Foamed concrete stability test

3.3.1 Static foam stability

No standardised foam stability test is available up to-date, but several researchers perform gravimetric or volumetric measurement for stability studies [14,33,34].

Since the densification of FC occurs by the gravity-driven solid particle migration of surrounding paste into the position of the disappeared bubble if an instable bubble breaks, the densities at different stages should be recorded on regular basis throughout the mixing and casting process. Density is measured by casting a 1 L sample into a known weight 100 mm cube mould, and weighing the captured sample. The measured weight with a unit volume is converted into the density and results in the following parameters: ρ_{base} – base mix density, ρ_{wet} – the wet density of FC that is measured as soon as a homogeneous FC is produced in the fresh state, and ρ_{mature} – the density obtained from 7-day aged sample kept in controlled air curing conditions (23±2^{o}C and 65±5% RH). The parameters allow determination of porosity parameters suggested by several researchers presented in Table 6 which indicates the stably captured foam volume as well as the void fraction after the final setting of the concrete.

Primarily, the measured wet density of FC is checked for the foam stability whether it falls within the tolerance of ±50 kg/m^3 from the desired target wet density [21,23]. Since the mature specimen may exhibit a notable degree of volumetric shrinkage during hydration which invalidates the density conversion, the volumetric change can be recorded by measuring the average dimensional change, at the midpoint of each side of the cube to determine.

The subsequent foam stability test is conducted by comparing the wet density and the mature density. This comparison can tell whether the entrained bubbles are secured in the surrounding mortar mix during the hydration process without a significant water loss released from the ruptured bubble film

other than the added mix water. Several empirical correlations between mature and wet density are presented in Table 7, and those will be compared with the obtained actual results.

Table 6. Various porosity calculation.

Reference	Porosity equation	Remarks
Wei *et al.* [23]	$\mathrm{n} = 1 - \frac{\rho_{mature}}{\rho_{base}}$	
Hoff[1] [35]	$\mathrm{n}_t = 1 - \frac{\rho_{wet}(1 + 0.20\gamma_c)}{(1 + w_c)\gamma_c\rho_w}$	n_t = theoretical porosity γ_c = specific weight of cement ρ_w = density of water
Nambiar *et al.*[2] [36]	$\mathrm{n}_t = 1 - \frac{\rho_{wet}(1 + 0.20\gamma_c + s_v)}{(1 + w_s)(1 + s_w)\gamma_c\rho_w}$	s_v = sand/cement ratio by weight s_w = sand/cement ratio by volume w_s = water/solids ratio by weight

[1] Theoretical porosity calculation by assuming 20% hydration bound.
[2] Expanded equation to account for filler (such as fly ash, sand, etc).

Table 7. Empirical correlation between mature and wet density of FC.

Reference	Model equation	Remarks
Wei *et al.* [37]	$\rho_{mature} = 1.000\rho_{wet} - 42.947$	Studied density: 300 – 1900 kg/m^3
Falliano *et al.* [38]	$\rho_{mature} = 0.809\rho_{wet} + 27.624$	Studied density: 400 – 1000 kg/m^3

3.3.2 Dynamic foam stability

External dynamic loading is imposed on FC through 3DCP pumping process, namely agitation in the hopper and pressure build-up within the transport channel, in the second stage of the experimental work. Assuming secured foam stability of tested samples discussed in Section 3.3.1, the comparison of pre- and post-pumped densities is the primary work in this section. The wet and mature post-pumped densities are denoted $\rho_{wet.pump}$ and $\rho_{mature\ pump}$ according to the age at the density measurement.

A laboratory scale gantry 3D concrete printer with a build volume of approximately 1 cubic metre is located in Stellenbosch University [39]. The 3D concrete printer is paired with a three-phase 380V 3kW progressive cavity concrete pump allowing a maximum aggregate size of 4 mm. The 3D concrete printer setup and pump detail with components are presented in Fig. 3.

Since the foam stability of FC for additive manufacturing application is of particular interest in this study, the density alteration resulting from the actual 3D concrete printer setup is a crucial parameter to

replicate 3DCP situation. Freshly prepared FC is placed in the hopper of the pump, and the material is transported through the 25-mm diameter sized hose. The end nozzle is lifted to 150 mm in height to catch the post-pumped material. The density of the post-pumped FC is captured at various feed durations to track the evolution of density change over time.

(a)

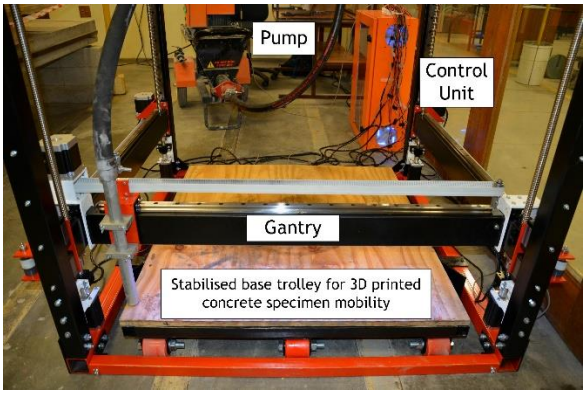

(b)

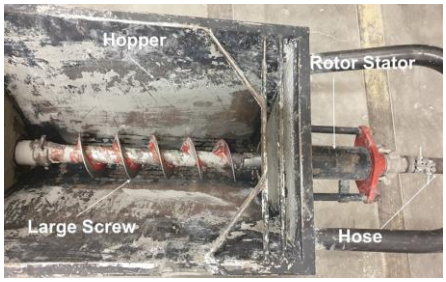

Fig. 3. (a) 3D concrete printer setup situated in Stellenbosch University [39]; (b) Rockcrete TSL progressive cavity pump indicating the rotor stator, hopper, hose and large screw [31].

3.4 Void structure analysis

Before and after extruded samples of TD-7, TD-10 and TD-14 were cast into cylindrical hollow 3D printed polylactic acid (common term, PLA) moulds with 20-mm inner diameter, 40-mm height and 0.4 mm wall thickness. The cast samples were stored for 7 days in the same air curing condition specified in Section 3.3.1.

Hardened samples, without removing PLA moulds, were subjected to X-ray computed tomography (CT) scan at the Stellenbosch CT Scanner Facility [40], using a General Electric VTomeX L240 system. The scans were done at 160 kV, 150µA and 25 µm voxel size with copper beam filtration of 0.1 mm to reduce beam hardening artefacts. The 2400 images, recorded during one 360-degree rotation of the sample, were acquired at 500 ms per image and 2000 rotation steps. The detailed procedure can be found in [41]. Visualization and analysis were performed with Volume Graphics VGStudioMax 3.4, as can be seen in Fig. 4. The software package allows for defect analysis, allowing assessment of the average porosity and pore counts, and foam structure analysis, providing pore size distribution and air void size characterisation along the height. It must be mentioned that the porosity and sphericity were analysed by taking 6 differently positioned disks, a size of 10 mm diameter and 3 mm high, along the

length of the sample into account. The averaged porosity, sphericity and coefficient of variations are reported in the following section.

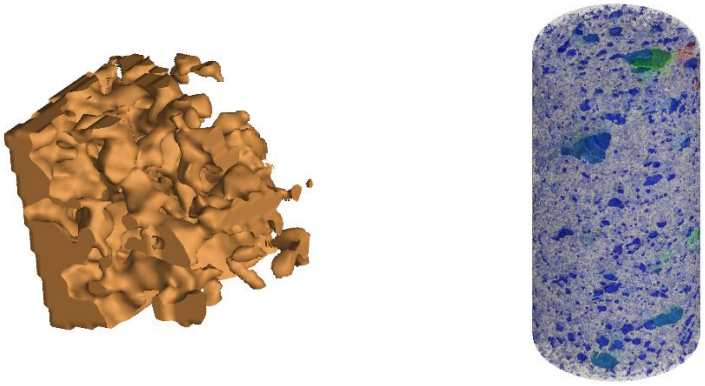

(a) (b)

Fig. 4. X-ray tomography scanned FC. (a) 3D visualised image for defect analysis; (b) foam structure analysis outcome.

4 Result and discussion

4.1 Fresh state characterisation of base mix

This section reports rheometer results of the base mixes for the different slump flows discussed in previous sections. Table 8 summarizes initial static ($\tau_{S,i}$) and dynamic yield stresses ($\tau_{D,i}$), re-flocculation rate (R_{thix}), structuration rate (A_{thix}), dynamic yield stress from flow curve ($\tau_{D.0}$), and plastic viscosity (μ_p) of BM180, BM180CSA, BM200 and BM220. A series of stress growth curves for the samples can be found in Fig. 5 (a) showing inversely correlated relationships between slump flow and yield stress, and flow curve is presented in Fig. 5 (b) showing similar trends than the stress growth curve results except for BM180CSA. Even though time-dependent thixotropy parameters (R_{thix} and A_{thix}) are not a particular interest in this study since base mix is immediately mixed with foam during FC production, this still shows outstandingly improved thixotropic behaviour of mixture containing CSA cement. Thus, it is believed the inclusion of CSA cement promotes the printability of FC.

Plastic viscosity of the sample is plotted in Fig. 5 (c). It is hard to explain the plastic viscosity depreciation in BM180CSA compared to BM180 having the same slump flow values, or stiffness where CSA inclusion normally increases viscosity of the bulk material according to [42,43]. This may be

because of the single batch for rheometer test only. Thus, a repetition is encouraged for better representation.

Table 8. Rheological characterisation of base mixes with different slump flows.

Sample	S[a] (mm)	$\tau_{S,i}$ [b] (Pa)	$\tau_{D,i}$ [c] (Pa)	R_{thix} (Pa/s)	A_{thix} (Pa/s)	μ_p [e] (Pa.s)
BM220	221.5	204.9	128.2	Not measured	Not measured	0.5
BM200	195	449.3	335.8	0.101	0.026	1.6
BM180	180	993.1	759.4	0.138	0.157	2.5
BM180CSA	180	1505.4	980.5	0.692	2.12	1.8

[a]Slump flow; [b]Initial static yield stress; [c]Initial dynamic yield stress; [d] Plastic viscosity.

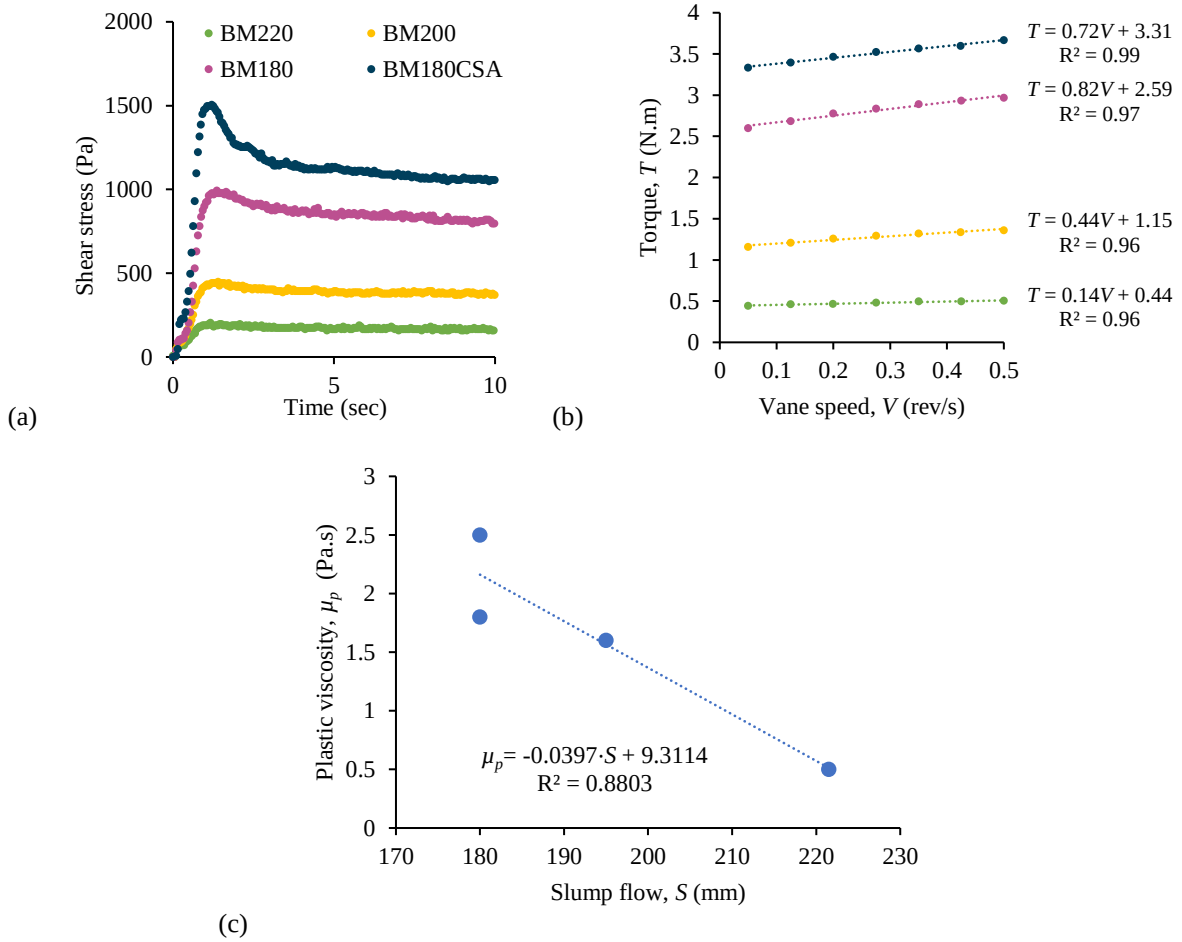

Fig. 5. (a) stress growth test results; (b) flow curve test results; (c) plastic viscosity of various slump flows.

Feneuil *et al.* [1] presented critical yield stress values depending on the bubble size which causes drainage and ripening destabilisation mechanisms in cement foam. Once the yield stress of bulk material exceeds the critical yield stress, the bulk material captures the movement of bubbles and no or negligible drainage and ripening may occur. For bubbles with a diameter of 100 µm and surface tension of 0.03

N/m, as presented in the study, the critical yield stress where ripening is the dominant destabilisation mechanism is calculated to be 300 Pa.

Thus, the assumption of no ripening and drainage is valid for BM200, BM180 and BM180CSA, and it can be seen that coalescence is the dominant destabilisation mechanism. The same study also mentioned about coalescence that film breakage may occur even when the capillary pressure does not exceed disjoining pressure due to dynamics during bubble rearrangement. It is, therefore, hypothesised that the highly stiff mortar having high yield stress, like the studied base mixes, leads to significant coalescence by the combination of large capillary pressure and kinetic energy.

4.2 Foamed concrete stability test

Prior to the stability test, the incorporated actual foam volume for each 10-litre batch of FC mix was recorded for BM220, BM200, BM180, and BM180CSA based on sensitivity analysis. Once the base mix is prepared, 50 – 80% of foam (by volume) is added according to the mix design – no foam breakdown occurrence situation. In the density check, the mixture is accepted if it is within the tolerance, i.e. ±50 kg/m^3 of the target density. In case the density is lower than the tolerance, the mixture is discarded while more foam is added when the density is higher than the tolerance. The process is iterated until the mixture is within the tolerance and the recorded foam volume is plotted in Fig. 6.

Due to the tolerance, the measured foam amounts of each mixture are linearly normalised by the density offset to the target density. The result shows TD-14 is the most sensitive sample to the fluidity of the base mix by presenting a steep gradient in the trendline, while TD-7 and TD-10 have relatively flattened gradients. The ranges of added foam volume are 4.58 – 5.23 L for TD-7, 3.54 – 3.90 L for TD-10, and 1.59 – 3.53 L for TD-14 per each 10 L batch. It must be clarified that the amount of foam volume incorporated into FC mixture is not necessarily equivalent or analogous to the actual foam fraction of FC since the incorporated foam is partially degraded when mixed by several factors.

The degraded foam volume increase when it is mixed with a stiffer base mix with a higher static yield stress and viscosity due to the higher potential energy, particularly in a dynamic environment such as when cement particles migrate for the foam insertion. When the energy transferred to the bubble

exceeds a threshold, breaching the ultimate strength of the film, the bubble rupture propagates, and it leads to failure of the bubble.

Moreover, the stiffer base mix has low fluidity, containing a higher volume of unsaturated cement grains. The unsaturated cement grains have better wettability, smaller contact angle due to the hydrophilicity and greater total surface free energy which attracts a greater number of water molecules for adsorption [44]. In other words, stronger attachment is expected for a higher surface energy solid grain, e.g. unsaturated cement grain, due to hydrogen bonds and van der Waals forces. At the contact between the unsaturated cement grain and a thin film with low free water condition, the unsaturated cement grain is thus postulated to withdraw liquid on or from the bubble film surface due to the high surface free energy. Moreover, the smaller contact angle promotes capillary pressure at contact [7], which leads to further bubble film thinning process.

When the bubble film ruptures, in general, the liquid inside of the bubble film is released, and it increases the liquid fraction of the bulk material. As the fluidity of the bulk material increases, the strain energy of the cementitious bulk material is lowered until it reaches the ultimate strength of the bubble film, which can be called *ideal fluidity*, allowing eased placement and dispersion of foam into the bulk material without a major degradation. This mechanism is argued to be the reason behind the inversely proportional relation between foam volume addition and slump flow of TD-14 in Fig. 6. It should be mentioned that the dataset presented in Fig. 6 represents the results based on the 10 L FC batch, and the linear scalability for the larger volume has not been validated.

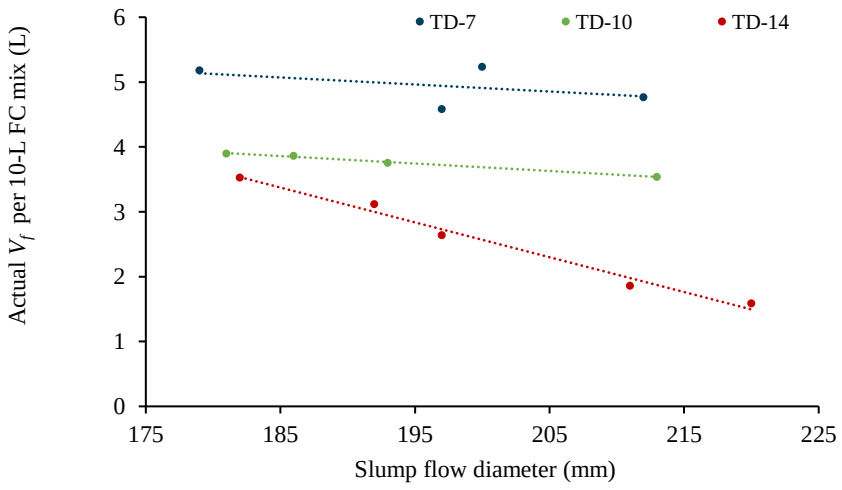

Fig. 6. Actual incorporated foam volume for 10-L FC batch with fluidity variation in base mix.

4.2.1 Stability under normal condition

Based on the observation above, various FC mixes, namely BM180, BM180CSA, BM200 and BM220, were prepared to investigate the stability through mature and wet density comparison and porosity. The design wet target density of the sample was set to be 700 kg/m^3 since it is generally more difficult to secure the stability for FC with lower density. Table 9 presents the actual wet and mature density for various base mix designs.

The result shows the wet densities of all the samples fall within the tolerable region to the target density, i.e. 650 – 750 kg/m^3. While BM180CSA shows the highest density reduction, which is -48.9 kg/m^3 or -6.9%, no significant defect or volumetric instability was found in the dry specimens by observation.

Table 9 also shows computed mature densities based on the various empirical models calculated by the actual wet density, and Fig. 7 (a) shows the mature-to-wet density ratios. The model of Wei *et al.* presents the closest trends over the samples in which there is only limited discrepancy (< 12%) with Falliano's model. Fig. 7 (b) presents the empirical correlation between the mature and wet density obtained in this study. By assuming the sample volume remained unchanged, the mass reductions are seemingly in a reasonable range by the comparison. This result supports the security of foam stability within a stiff base mix and the compatibility of CSA cement in FC, thus BM180CSA was selected for the upcoming study, considering foam stability and printability.

Table 9. Actual wet and mature densities (Units are in kg/m^3).

Sample	Actual ρ_{wet}	Actual ρ_{mature}	Wei *et al.* ρ_{mature}	Falliano *et al.* ρ_{mature}
BM180CSA	704.8	655.9	661.9	597.8
BM180	691.3	670.7	648.4	586.9
BM200	681.8	655.3	638.8	579.2
BM220	694.8	666.3	651.8	589.7

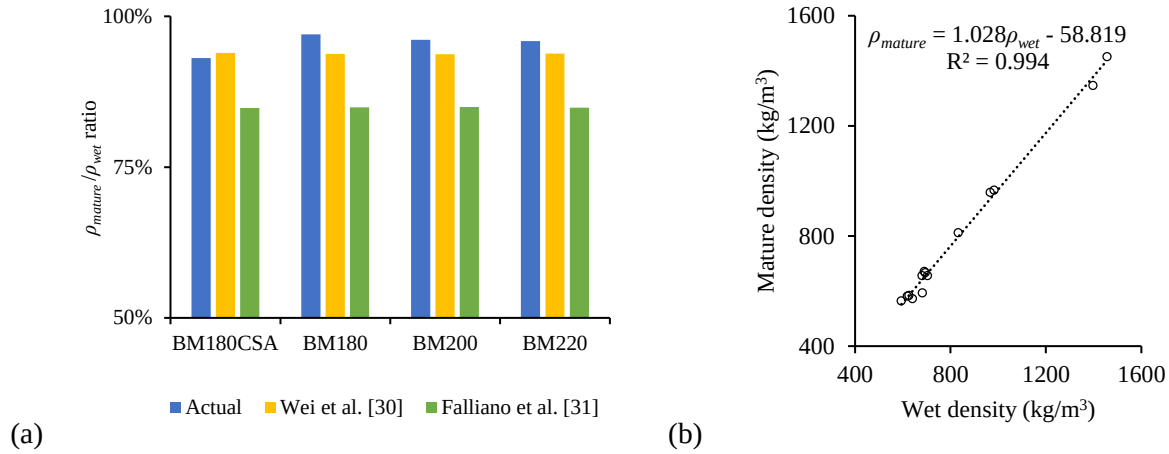

Fig. 7. (a) Mature-to-wet density ratio comparison with various empirical model (b) correlation between actual mature and actual wet density.

With the selected base mix, various FC samples with different target densities were prepared and the physical property of FC results are summarised in Table 10. Comparing the wet density measured in the fresh state with wet target density is an initial stability check, and all the samples were within an acceptable density range. Volumetric changes during the setting period are shown in Table 10. In overall, the density conversion from the casted cube specimen is valid as the volumetric changes seem to be insignificant.

Various measured and theoretical porosities are shown in Table 10. For Nambiar *et al.*'s theoretical porosity model, fly ash, silica fume, nano silica, and fine sands are considered as a filler as per the literature [36]. Since Hoff's model only considers cement, water and foam, other constituents are completely ignored which leads to imbalance of total volume and mass. While the theoretical porosities calculated with the equations proposed by Hoff and Nambiar *et al.* are similar to each other, they are significantly higher than porosity model proposed by Wei *et al.*, with the difference increasing as the target density increases. These parameters are further discussed with measured porosity from the void structure analysis results in Section 4.3.

Fig. 8 shows the comparison between the actual mature-to-wet density ratio and the ratio computed based on various empirical models. Providing volumetric stability of the specimen, there is no notable mass reduction between the casting and mature densities. Based on the discussed results and observations, the slump flow under 185 mm after 15 strokes increases the possibility of instability

because the base mix is too stiff, i.e. too low fluidity, where the slump flow higher than 195 mm is not favourable to printability according to [3].

Table 10. Physical properties of fresh and hardened state FC with different target densities (Coefficient of variations in brackets).

	ρ_{base} (kg/m^3)	ρ_{wet} (kg/m^3)	ρ_{mature} (kg/m^3)	Wei *et al.* *n* (%)	Hoff *n* (%)	Nambiar *et al.* *n* (%)	*dV* (%)
TD-7	1796.0	704.8 (0.0195)	655.9 (0.0198)	63.5	73.0	73.3	-0.63
TD-10	1776.0	967.3 (0.0298)	958.6 (0.0246)	46.0	62.9	63.1	+0.79
TD-14	1784.0	1397.8 (0.0115)	1346.0 (0.0127)	24.6	46.4	46.3	-0.36

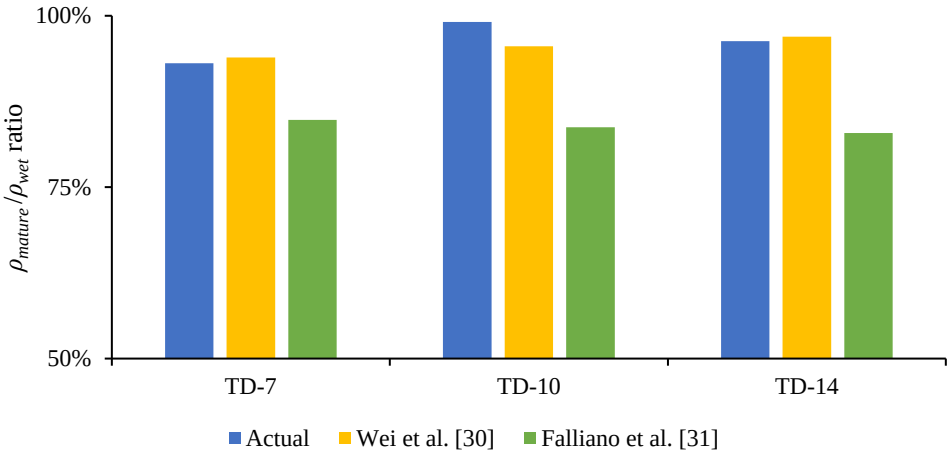

Fig. 8. Mature-to-wet density ratio of various empirical model.

4.2.2 Stability under external pressure

Providing foam stability of FC with a wide density range in static condition, foam stability under high pressure has been investigated with the concrete pump used for the 3D concrete printer. Pre-pressure (ρ_{wet}) and post-pressure density ($\rho_{wet.pump}$) measurements are presented in Fig. 9 (a) – (c) for TD-7, TD-10, and TD-14, respectively. Solid lines represent ρ_{wet} measured from the mixing container when fresh FC material is prepared. $\rho_{wet.pump}$'s are shown as dots in the figure with three different pumping feed durations for better representability in the continuous pumping process of 3DCP. Dashed lines indicate the upper/lower boundaries of the tolerance to the target density.

The results show that TD-7 is the most stable sample under pumping pressure condition by showing only a subtle difference in density with pumping duration, and all densities are within the tolerance

boundaries. It may be contributed by the “cushioning effect” impeding the intensity of external disturbance which is more prominent in bulk material with higher foam volume fraction [45]. While foam stability is shown in the pre-pressure density of TD-14, the post-pressure densities are unacceptable, even for the initial post-pressure density. In most concrete pumping processes, the lubricating layer is formed between the pipe wall and the bulk material. The yield stress and plastic viscosity of the lubrication layers are considered as about one fifth and one fifteenth of the bulk material, respectively [19]. Since the rheological properties and the thickness of lubrication layer are inherited by the parental material, the lubrication layer of TD-14 is expected to have higher yield stress and plastic viscosity which has higher solid concentration leading to higher rheological parameters [46]. This results in the build-up of higher internal stress than TD-7 which can be a cause of foam instability for TD-14. The pre-pressure density as well as the initial post-pressure density of TD-10 are acceptable, even though the following post-pressure densities have rapidly increased density, which are outside the tolerance. In this case, a continuous concrete mixer can be a remedy.

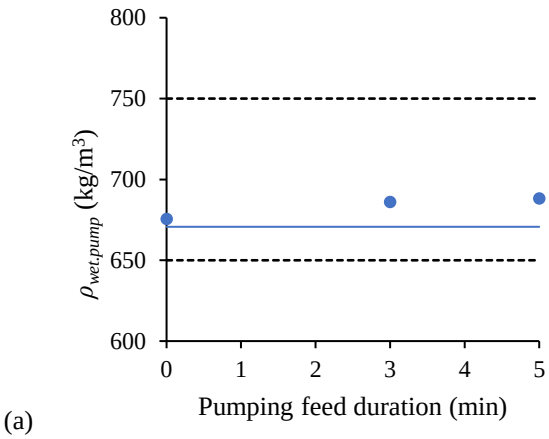

(a)

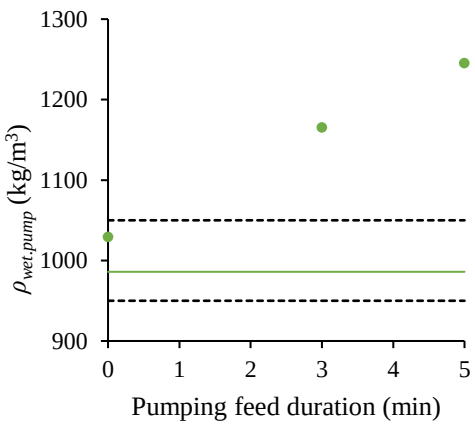

(b)

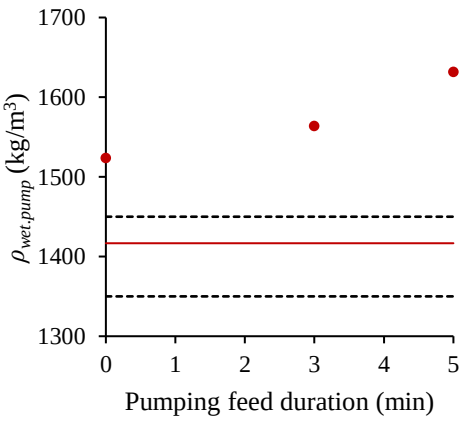

(c)

Fig. 9. Foam stability check under pumping pressure. ρ_{wet} – solid line and $\rho_{wet.pump}$ – three dots for (a) TD-7, (b) TD-10, and (c) TD-14.

From the observation above, the rheology of bulk material is one of the key factors for the foam stability, in particular, under the pumping pressure condition. Hence, it is recommended that, if the FC is designed to be pumped, the rheology of TD-14 should be adapted by adjusting the water-to-solid ratio to reduce the solid concentration.

4.3 Void structure analysis

Cross-sectional images produced by three-dimensional X-CT scans of samples are shown in Fig. 10. These images were used to calculate the mean void fraction in each sample, and the result is shown in Table 11. The table also contains the mean sphericity of each scanned sample. The result shows porosity reduction in each target density in the post-pump samples, which is directly linked to the density increase discussed in Section 4.1. It is not easy to assess the foam stability by the obtained porosity directly, however the TD-10 post-pump sample is deemed to have foam instability due to the significant porositiy reduction compared to the other samples.

The measured pre- and post-pumped porosities are compared with the porosity models discussed in the Section 3.3.1. The calculated porosity and theoretical porosities are plotted against the measured pre- and post-pumped porosity which can be found in Fig. 11, with the unity line as a dotted line. Theoretical porosities still show the largest discrepancy to the measured porosities while the computed porosity proposed by Wei *et al.* is close to the unity line for the pre-pumped porosity. However, the latter model also shows the deviation in the plot against post-pumped porosity. The inconsistency is due to the porosity drop through the pumping process while the computed porosities remained unchanged.

It is postulated that the material transport procedure through the pump pipe lowers the sphericity by confinement as reported in the literature [47]. This is however not true for TD 7, where the sphericity increased as a result of pumping. These results seem to indicate that the low density FC would be perfectly suited for 3D printing, as the quality of the voids in the cement improves when pumping takes place.

Fig. 12 presents pore size frequency distributions of pre- and post-pumped FC samples with different target densities. All distributions are significantly skewed to the right, meaning smaller pore diameter/size, mainly 100 – 400 μm in diameter, are dominant in the matrix. Post-pump TD-7 and TD-10 samples contain slightly smaller sized pores than pre-pump samples, while only negligible change is found in TD-14 samples. Similar tendency is also shown when it comes to an average void size comparison between pre- and post-pumped samples. Bubble size is highly dependent on applied pressure to the bubble. Since post-pump samples have experienced extra pumping pressure, the smaller pore fraction is expected to be higher than in the pre-pump sample.

Table 11. Mean porosity and sphericity results from XCT analysis. (Coefficient of variation in brackets.)

		TD-7	TD-10	TD-14
Porosity	Pre-pump	52.77% (0.186)	33.62% (0.2190)	19.94% (0.1003)
	Post-pump	52.31% (0.1112)	22.20% (0.1592)	16.07% (0.1571)
Sphericity	Pre-pump	0.596 (0.0106)	0.619 (0.0054)	0.544 (0.0071)
	Post-pump	0.604 (0.0097)	0.535 (0.0153)	0.536 (0.0074)

	TD-7	TD-10	TD-14
Pre-pump	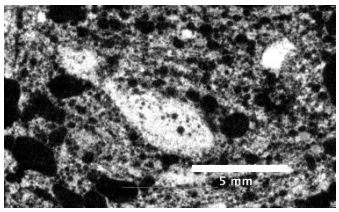	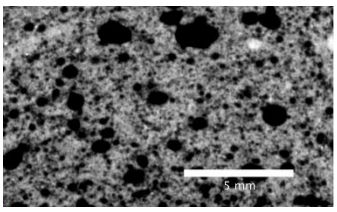	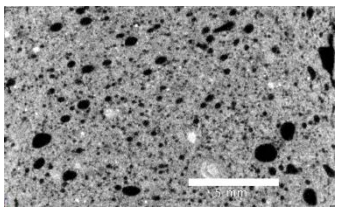
Post-pump	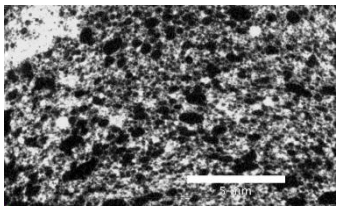	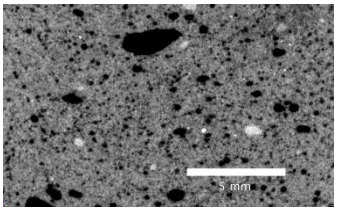	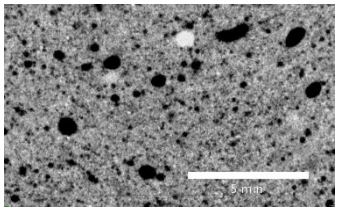

Fig. 10. 2D cross-section image of hardened pre- and post-pump FC obtained by X-ray tomography.

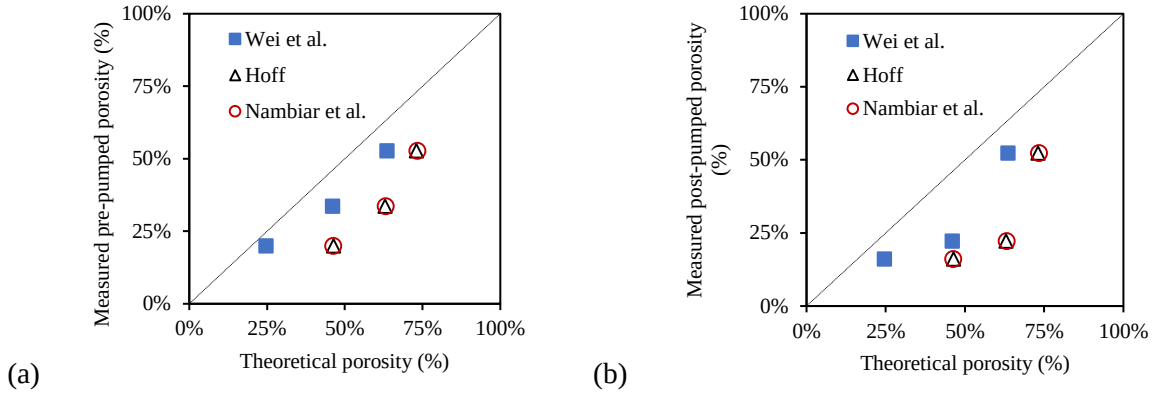

Fig. 11. Computed theoretical porosity plot against (a) measured pre-pumped porosity, and (b) measured post-pumped porosity. The average void diameter, denoted as $\bar{x}$, is specified in the graphs.

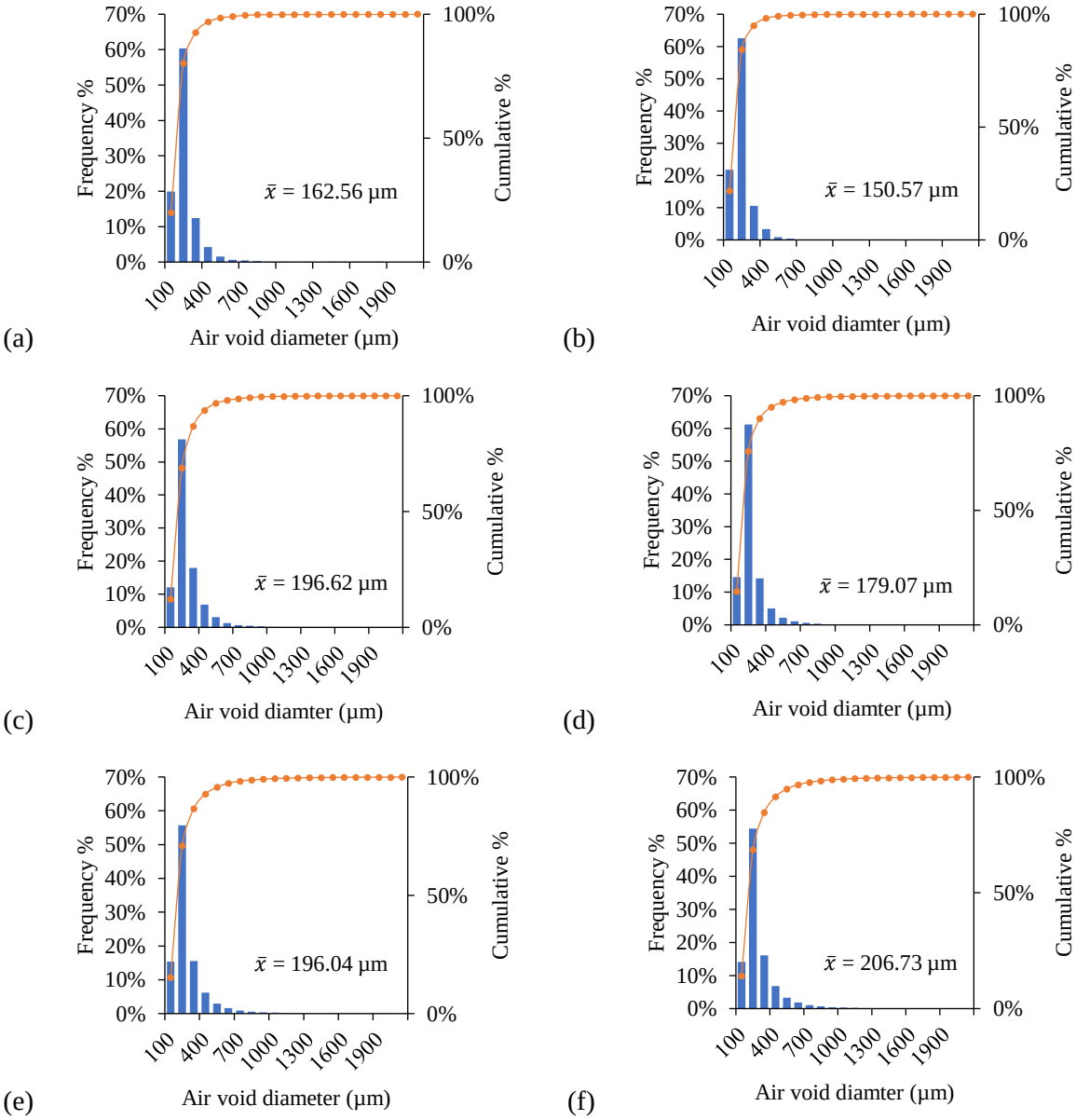

Fig. 12. Pore size distribution of (a) pre-pump TD-7, (b) post-pump TD-7, (c) pre-pump TD-10, (d) post-pump TD-10, (e) pre-pump TD-14, and (f) post-pump TD-14.

5 Conclusion

Stability assessment of a novel additive manufacturing application of FC and foam destabilisation mechanisms under dynamic condition, i.e. pumping, are reported in this paper in a comprehensive manner. It is hypothesised that coalescence is the dominant foam destabilisation mechanism for a relatively stiff concrete mix with static yield shear stress of 100 Pa or more, noting that current literature on stability of FC mainly reports ripening and drainage mechanisms in base mixes with yield stress of 10 – 100 Pa.

Obtaining the most appropriate stiffness for the base mix, to satisfy foam stability and buildability, is challenging for developing 3DP-FC due to the contrasting nature of these characteristics. FC with target density of 700 kg/m^3 was produced with various base mixes and all samples showed stability in the first phase of the study. The influence of external pressure on foam stability in a density range of 700 to 1400 kg/m^3 was subsequently investigated. The key findings about the second part of the study are as follows:

- The higher foam volume fraction sample, i.e. lower density TD-7 and TD-10, showed better foam stability regardless of the stiffness of the fresh base mix. Foam stability of TD-14 was sensitive to the base mix stiffness. The released liquid by foam breakage increases the fluidity, causing a decrease in yield stress, until the equilibrium state where no further major foam degradation occurs.
- In this study, a base mix slump flow of 200 mm and yield shear stress of 450 Pa showed the best foam stability for all three densities (700, 1000, 1400 kg/m^3). However, for these FC mixes, the 3D printing buildability is not favourable. The slump flow range of 185 – 195 mm is recommended for a reasonable buildability by observation.
- The cushioning effect prevents notable foam degradation in TD-7 during pumping due to high foam volume fraction (> 60%).

- TD-10 and TD-14 undergo notable densification throughout pumping, and the post-pump densities are eventually outside a predetermined tolerance. Continuous mixing instead of batch mixing, base mix stiffness modification are foreseen remedies and the subject of continued research towards stable 3DP-FC.
- A dominant pore size of 100 – 400 μm in diameter was found by void structure analysis. Pumping pressure increased the sphericity and reduced void size of TD-7, which is an indication of high-quality foam.

Since an overall longer open time in the hopper for pumping tends to affect foam stability, it is recommended to investigate the similar study with a continuous pump.

Declaration of competing interest

None.

CRediT authorship contribution statement

Seung Cho: Conceptualisation, Data curation, Methodology, Formal analysis, Validation, Writing – original draft, Visualisation, Investigation. **Algurnon van Rooyen**: Conceptualisation, Supervision, Writing – review & editing. **Elsabe Kearsley**: Conceptualisation, Data curation, Investigation, Writing – review & editing. **Gideon van Zijl**: Conceptualisation, Supervision, Writing – review & editing, Project administration, Funding acquisition.

Acknowledgements

Cathay Industries (Africa) is acknowledged for providing CSA cement. The research is supported by The Concrete Institute in South Africa.

References

[1] B. Feneuil, P. Aimedieu, M. Scheel, J. Perrin, N. Roussel, O. Pitois, Stability criterion for fresh cement foams, Cement and Concrete Research. 125 (2019) 105865. https://doi.org/https://doi.org/10.1016/j.cemconres.2019.105865.

[2] S.C. Paul, G.P.A.G. van Zijl, I. Gibson, A Review of 3D Concrete Printing Systems and Materials Properties : Current Status and Future Research Prospects, Rapid Prototyping Journal. 24 (2018) 784–798. https://doi.org/10.1108/RPJ-09-2016-0154.

[3] S. Cho, J. Kruger, A. van Rooyen, G. van Zijl, Rheology and application of buoyant foam concrete for digital fabrication, Composites Part B: Engineering. 215 (2021) 108800. https://doi.org/https://doi.org/10.1016/j.compositesb.2021.108800.

[4] V. Markin, V.N. Nerella, C. Schröfl, G. Guseynova, V. Mechtcherine, Material design and performance evaluation of foam concrete for digital fabrication, Materials. 12 (2019). https://doi.org/10.3390/ma12152433.

[5] D. Falliano, D. De Domenico, G. Ricciardi, E. Gugliandolo, 3D-printable lightweight foamed concrete and comparison with classical foamed concrete in terms of fresh state properties and mechanical strength, Construction and Building Materials. 254 (2020) 119271. https://doi.org/10.1016/j.conbuildmat.2020.119271.

[6] A. Fameau, A. Salonen, Effect of particles and aggregated structures on the foam stability and aging, Comptes Rendus Physique. 15 (2014) 748–760. https://doi.org/10.1016/j.crhy.2014.09.009.

[7] H.J. Butt, K. Graf, M. Kappl, Physics and Chemistry of Interfaces, Second Ed., Wiley, California, 2003. https://doi.org/doi:10.1002/3527602313.ch6.

[8] R.J. Pugh, Foaming , foam films , antifoaming and defoaming, Advances in Colloid and Interface Science. 64 (1996) 67–142. https://doi.org/https://doi.org/10.1016/0001-8686(95)00280-4.

[9] C.M. Phan, A. V. Nguyen, J.D. Miller, G.M. Evans, G.J. Jameson, Investigations of bubble-particle interactions, International Journal of Mineral Processing. 72 (2003) 239–254. https://doi.org/10.1016/S0301-7516(03)00102-9.

[10] L. Wang, R. Yoon, Effects of surface forces and film elasticity on foam stability, International Journal of Mineral Processing. 85 (2008) 101–110. https://doi.org/10.1016/j.minpro.2007.08.009.

[11] P. Basařová, M. Zedníková, Effect of Surfactants on Bubble-Particle Interactions, in: Ashim Kumar Dutta (Ed.), Surfactants and Detergents, IntechOpen, 2019. https://doi.org/10.5772/intechopen.85436.

[12] B. V Derjaguin, N. V Churaev, V.M. Muller, Surface Forces, Springer, New York, 1987.

[13] A.S. Aronson, V. Bergeron, M.E. Fagan, C.J. Radke, The influence of disjoining pressure on foam stability and flow in porous media, Colloids and Surfaces A: Physicochemical and Engineering Aspects. 83 (1994) 109–120. https://doi.org/https://doi.org/10.1016/0927-7757(94)80094-4.

[14] M.R. Jones, L. Zheng, K. Ozlutas, Stability and instability of foamed concrete, Magazine of Concrete Research. 68 (2016) 542–549. https://doi.org/10.1680/macr.15.00097.

[15] V. Markin, I. Ivanova, S. Fataei, S. Reißig, V. Mechtcherine, Investigation on Structural Build-Up of 3D Printable Foam Concrete BT - Second RILEM International Conference on Concrete and Digital Fabrication, in: F.P. Bos, S.S. Lucas, R.J.M. Wolfs, T.A.M. Salet (Eds.), Springer International Publishing, Cham, 2020: pp. 301–311.

[16] B. Feneuil, N. Roussel, O. Pitois, Yield stress of aerated cement paste, Cement and Concrete Research. 127 (2020) 105922. https://doi.org/https://doi.org/10.1016/j.cemconres.2019.105922.

[17] M. Lessard, M. Baalbaki, P.-C. Aïtcin, Effect of Pumping on Air Characteristics of Conventional Concrete, Transportation Research Record. 1532 (1996) 9–14. https://doi.org/10.1177/0361198196153200102.

[18] K.C. Hover, R.J. Phares, Impact of Concrete Placing Method on Air Content, Air-Void System Parameters, and Freeze-Thaw Durability, Transportation Research Record. 1532 (1996) 1–8. https://doi.org/10.1177/0361198196153200101.

[19] V. Mechtcherine, F.P. Bos, A. Perrot, W.R.L. da Silva, V.N. Nerella, S. Fataei, R.J.M. Wolfs, M. Sonebi, N. Roussel, Extrusion-based additive manufacturing with cement-based materials – Production steps, processes, and their underlying physics: A review, Cement and Concrete Research. 132 (2020) 106037. https://doi.org/10.1016/j.cemconres.2020.106037.

[20] B. Panda, S.C. Paul, M.J. Tan, Anisotropic mechanical performance of 3D printed fiber reinforced sustainable construction material, Materials Letters. 209 (2017) 146–149. https://doi.org/https://doi.org/10.1016/j.matlet.2017.07.123.

[21] E. Kearsley, D. Mostert, Designing mix composition of foamed concrete with high fly ash contents, in: Use of Foamed Concrete in Construction, Thomas Telford Publishing, 2005: pp. 29–36. https://doi.org/10.1680/uofcic.34068.0004.

[22] B. Feneuil, N. Roussel, O. Pitois, Optimal cement paste yield stress for the production of stable cement foams, Cement and Concrete Research. 120 (2019) 142–151. https://doi.org/https://doi.org/10.1016/j.cemconres.2019.03.002.

[23] S. Wei, C. Yiqiang, Z. Yunsheng, M.R. Jones, Characterization and simulation of microstructure and thermal properties of foamed concrete, Construction and Building Materials. 47 (2013) 1278–1291. https://doi.org/10.1016/j.conbuildmat.2013.06.027.

[24] A.S. van Rooyen, Mechanics and durability of surface treated structural foamed concrete, PhD Dissertation, Stellenbosch University, 2020.

[25] M.R. Jones, A. McCarthy, Utilising unprocessed low-lime coal fly ash in foamed concrete, Fuel. 84 (2005) 1398–1409. https://doi.org/10.1016/j.fuel.2004.09.030.

[26] E.K.K. Nambiar, K. Ramamurthy, Influence of filler type on the properties of foam concrete, 28 (2006) 475–480. https://doi.org/10.1016/j.cemconcomp.2005.12.001.

[27] ASTM International, ASTM C1437-15 Standard Test Method for Flow of Hydraulic Cement Mortar, 2015. https://doi.org/10.1520/C1437-15.

[28] South African National Standard, SANS 50197-1 Part 1 : Composition , specifications and conformity criteria for common cements, 2013.

[29] Germann Instrument, ICAR Rheometer, (2013) 5. http://germann.org/products-by-application/rheology-of-concrete/icar-rheometer (accessed February 19, 2021).

[30] N. Roussel, A thixotropy model for fresh fluid concretes: Theory, validation and applications, Cement and Concrete Research. 36 (2006) 1797–1806. https://doi.org/https://doi.org/10.1016/j.cemconres.2006.05.025.

[31] J. Kruger, S. Zeranka, G. van Zijl, An ab initio approach for thixotropy characterisation of (nanoparticle-infused) 3D printable concrete, Construction and Building Materials. 224 (2019) 372–386. https://doi.org/10.1016/j.conbuildmat.2019.07.078.

[32] Y. Qian, S. Kawashima, Distinguishing dynamic and static yield stress of fresh cement mortars through thixotropy, Cement and Concrete Composites. 86 (2018) 288–296. https://doi.org/10.1016/j.cemconcomp.2017.11.019.

[33] W. She, Y. Du, G. Zhao, P. Feng, Y. Zhang, X. Cao, Influence of coarse fly ash on the performance of foam concrete and its application in high-speed railway roadbeds, Construction and Building Materials. 170 (2018). https://doi.org/10.1016/j.conbuildmat.2018.02.207.

[34] K. Dhasindrakrishna, K. Pasupathy, S. Ramakrishnan, J. Sanjayan, Effect of yield stress development on the foam-stability of aerated geopolymer concrete, Cement and Concrete Research. 138 (2020) 106233. https://doi.org/10.1016/j.cemconres.2020.106233.

[35] G.C. Hoff, Porosity-strength considerations for cellular concrete, Cement and Concrete Research. 2 (1972) 91–100. https://doi.org/10.1016/0008-8846(72)90026-9.

[36] E.K.K. Nambiar, K. Ramamurthy, Models for strength prediction of foam concrete, Materials and Structures/Materiaux et Constructions. 41 (2008) 247–254. https://doi.org/10.1617/s11527-007-9234-0.

[37] S. Wei, C. Yiqiang, Z. Yunsheng, M.R. Jones, Characterization and simulation of microstructure and thermal properties of foamed concrete, Construction and Building Materials. 47 (2013) 1278–1291. https://doi.org/https://doi.org/10.1016/j.conbuildmat.2013.06.027.

[38] D. Falliano, D. De Domenico, G. Ricciardi, E. Gugliandolo, Experimental investigation on the compressive strength of foamed concrete: Effect of curing conditions, cement type, foaming agent and dry density, Construction and Building Materials. 165 (2018) 735–749. https://doi.org/10.1016/j.conbuildmat.2017.12.241.

[39] S. Cho, J. Kruger, S. Zeranka, G. van Zijl, 3D Printing Concrete Technology and Mechanics, Concrete Beton Technical Journal. (2019).

[40] A. du Plessis, S.G. le Roux, A. Guelpa, The CT Scanner Facility at Stellenbosch University: An open access X-ray computed tomography laboratory, Nuclear Instruments and Methods in Physics Research Section B: Beam Interactions with Materials and Atoms. 384 (2016) 42–49. https://doi.org/https://doi.org/10.1016/j.nimb.2016.08.005.

[41] A. du Plessis, B.J. Olawuyi, W.P. Boshoff, S.G. le Roux, Simple and fast porosity analysis of concrete using X-ray computed tomography, Materials and Structures. 49 (2016) 553–562. https://doi.org/10.1617/s11527-014-0519-9.

[42] G. Ke, J. Zhang, S. Xie, T. Pei, Rheological behavior of calcium sulfoaluminate cement paste with supplementary cementitious materials, Construction and Building Materials. 243 (2020) 118234. https://doi.org/https://doi.org/10.1016/j.conbuildmat.2020.118234.

[43] M. Chen, L. Li, Y. Zheng, P. Zhao, L. Lu, X. Cheng, Rheological and mechanical properties of admixtures modified 3D printing sulphoaluminate cementitious materials, Construction and Building Materials. 189 (2018) 601–611. https://doi.org/10.1016/j.conbuildmat.2018.09.037.

[44] N.S. Klein, J. Bachmann, A. Aguado, B. Toralles-Carbonari, Evaluation of the wettability of mortar component granular materials through contact angle measurements, Cement and Concrete Research. 42 (2012) 1611–1620. https://doi.org/10.1016/j.cemconres.2012.09.001.

[45] X. Zeng, X. Lan, H. Zhu, H. Liu, H.A. Umar, Y. Xie, G. Long, C. Ma, A review on bubble stability in fresh concrete: Mechanisms and main factors, Materials. 13 (2020) 1–24. https://doi.org/10.3390/MA13081820.

[46] M.S. Choi, Y.J. Kim, S.H. Kwon, Prediction on pipe flow of pumped concrete based on shear-induced particle migration, Cement and Concrete Research. 52 (2013) 216–224. https://doi.org/https://doi.org/10.1016/j.cemconres.2013.07.004.

[47] J. Kruger, A. du Plessis, G. van Zijl, An investigation into the porosity of extrusion-based 3D printed concrete, Additive Manufacturing. 37 (2021) 101740. https://doi.org/https://doi.org/10.1016/j.addma.2020.101740.